International Journal of Rock Mechanics & Mining Sciences 92 (2017) 19–29

Contents lists available at ScienceDirect

International Journal of Rock Mechanics & Mining Sciences

journal homepage: www.elsevier.com/locate/ijrmms

Discontinuous deformation analysis based on strain-rotation decomposition

Huo Fan[a,*], Hong Zheng[b], Jidong Zhao[a,*]

[a] Department of Civil and Environmental Engineering, The Hong Kong University of Science and Technology, Clear Water Bay, Kowloon, Hong Kong
[b] Key Laboratory of Urban Security and Disaster Engineering, Ministry of Education, Beijing University of Technology, Beijing 100124, China

ARTICLE INFO

Keywords:
Strain-rotation decomposition
Dynamic formulation
Discontinuous deformation analysis
Large rotation

ABSTRACT

The S-R (strain-rotation) decomposition theorem has an ability to capture strain components and rotation components at the same time. Using the principle of virtual power (VP), in this study, a new formulation independent of specific numerical methods is proposed for the analysis of dynamic large or small deformation. Then, the formulation is applied to the discontinuous deformation analysis (DDA), yielding a new DDA based on the S-R decomposition theorem, abbreviated as $SRDDA_{vp}$. Compared with the conventional DDA, $SRDDA_{vp}$ adopts a slightly modified basic variables together with the generalized-α method. The analysis of some typical examples indicates that $SRDDA_{vp}$ can naturally overcome the issue of volume expansion, effectively improve the calculation accuracy and, equip DDA with the potential to treat large deformation.

1. Introduction

The discontinuous deformation analysis (DDA) is a discrete block-based method [1,2]. In both 2D-DDA and 3D-DDA, the special shape functions and basic variables are employed to make the approximation of displacement field is independent of the shape of block. The effectiveness of DDA in geotechnical problems has been recognized [3–5], and extensively applied in the analysis of seismic landslides [6–8], crack propagations [9–11], hydraulic fractures [12,13], masonry structures [14], the path tracking of rockfalls [15], fluid-solid coupling [16] and motion of particulate media [17,18].

During the past 20 years, the performance of DDA is enhanced largely. The higher-order DDA [19], a nodal-based DDA [20], the FEM-DDA [21], the NMM-DDA [22] and the DDA with bonding springs [23] improved the deformability of objects simulated by DDA. The post-adjustment method [24], the Taylor series method [25], the trigonometric method [26], the post-contact adjustment method [27], the displacement-strain modification method [28] overcame the volume expansion of block due to small deformation assumption, and a procedure [29] to mitigate the elastic distortions with large rotation. Some convergence criterions [30], the trick of contact state recovery [31], and the strategy of strengthening the movement trend [32] speeded up the open-close iteration. The augmented Lagrange multiplier method [33], the Lagrange multiplier method [34], the complementarity method [35–37]the variational inequality method [38] improved the accuracy of contact force. The one temporary spring method [39] and the angle-based method [32] handled the indeterminacy of vertex-vertex contact. For 3D-DDA, the contact submatrices [40] modified the stiffness matrix. The models of point-to-face and edge-to-edge contact [41,42] dealt with the various contacts. An algorithm [43] coped with the frictionless vertex-to-face contacts. Another algorithm [44] searched and calculated geometrical contacts. A fast algorithm [45] identified the common plane. A multi-shell cover algorithm [46] detected contacts. A nodal-based 3D-DDA [47] was developed. Moreover, the new contact theory [48] developed by Shi is expected to significantly simplify the difficulties in treating three-dimensional singular contacts.

It is worth mentioning that the S-R decomposition theorem [49–54] is an important result in the field of geometric nonlinearity. By this theorem, the strain and local rotation can be simultaneously and accurately captured. However, a dynamic formulation based on this theorem remains absent. In this study, using the principle of virtual power (VP), a new formulation for dynamic analysis is firstly deduced. The S-R-D-based formulation is independent of specific numerical methods. In other words, it provides an opportunity to develop DDA under the background of the new theory, in which the small strain assumption is no longer needed. Compared with the conventional DDA, a slightly modified displacement function and the generalized-α[55] method are utilized in the S-R-D-based DDA, abbreviated by $SRDDA_{vp}$, in which the subscript “vp” stands for the principle of virtual power. The results obtained show that $SRDDA_{vp}$ can naturally overcome the issue of volume expansion, effectively improve the calculation accuracy and, equip DDA with the potential to treat large deformation.

* Corresponding author.
E-mail addresses: Huofan@ust.hk (H. Fan), jzhao@ust.hk (J. Zhao).

http://dx.doi.org/10.1016/j.ijrmms.2016.12.003
Received 4 March 2016; Received in revised form 17 November 2016; Accepted 7 December 2016
1365-1609/

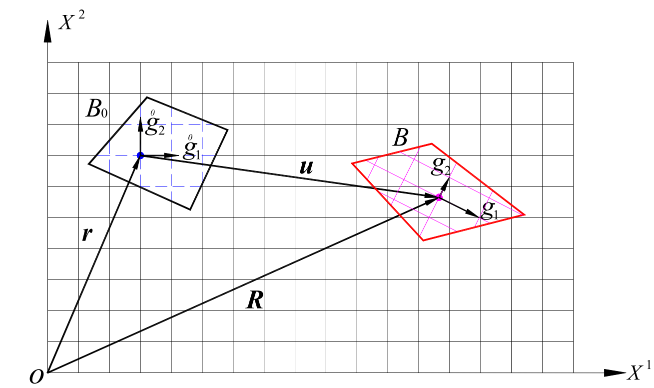

Fig. 1. Co-moving coordinate description of the motion of a deformable body.

2. S-R decomposition theorem

The S-R decomposition theorem is always associated with the co-moving coordinate description method. The connection between the theorem and the co-moving coordinate has been demonstrated and illuminated in [49–54]. Here, for completeness, we only touch upon the related concepts and theories.

For a deformable body in Euclidean space E^3, the following two reference frames are chosen to describe the motion of a body:

(1) A global reference system $\{X^i\}$ (i=1, 2, 3), which is fixed in space.
(2) A co-moving coordinate system $\{x^i\}$ (i=1, 2, 3), which is embedded in the deformable body, with its coordinate line allowed to stretch and rotate.

In general, the initial reference frame or the initial co-moving coordinate system is chosen as a rectilinear or curvilinear orthogonal system. However, owing to the occurrence of deformation of the considered body, a new curvilinear system may be formed following the deformation. Fig. 1 shows the configuration change of a co-moving coordinate system in the two-dimensional case. The situation in the three-dimensional case is similar. Let **r** and **R** be the position vectors of a point before and after deformation, and **u** the displacement vector. Then, the three vectors have the relationship

$$\mathbf{R} = \mathbf{r} + \mathbf{u}. \tag{1}$$

We define the basis vectors at a point in the initial co-moving coordinate system by

$$\overset{0}{\mathbf{g}}_i = \frac{\partial\ \mathbf{r}}{\partial\ x^{\ i}}, \quad i = 1,\ 2,\ 3. \tag{2}$$

After deformation, the basis vectors at the same point change to

$$\mathbf{g}_i = \frac{\partial\ \mathbf{R}}{\partial\ x^{\ i}}, \quad i = 1,\ 2,\ 3. \tag{3}$$

Using Eq. (1), one can obtain

$$\frac{\partial\ \mathbf{R}}{\partial\ x^{\ i}} = \frac{\partial\ \mathbf{r}}{\partial\ x^{\ i}} + \frac{\partial\ \mathbf{u}}{\partial\ x^{\ i}}. \tag{4}$$

In the curvilinear system, any vector can be decomposed with respect to the basis vector $\overset{0}{\mathbf{g}}_i$. For the displacement **u**, we have

$$\mathbf{u} = u^j \overset{0}{\mathbf{g}}_j \tag{5}$$

Further, we can obtain

$$\frac{\partial\ \mathbf{u}}{\partial\ x^{\ i}} = \frac{\partial}{\partial\ x^{\ i}}\left(u^{\ j}\overset{0}{\mathbf{g}}_j\right) = u^j|_{\ i}\overset{0}{\mathbf{g}}_j. \tag{6}$$

Then, the following transformation of basis vectors can be obtained

$$\mathbf{g}_i = F_i^j \overset{0}{\mathbf{g}}_j, \tag{7}$$

where F_i^j is a linear differential transformation function and can be described as

$$F_i^j = \delta_i^j + u^j|_{\ i}. \tag{8}$$

where $\delta_{\ i}^{\ j}$ is the Kronecker-delta. The covariant derivative $u^{\ j}|_i$ of displacement is expressed as

$$u^j|_{\ i} = \frac{\partial u^j}{\partial x^i} + \overset{0}{\mathbf{\Gamma}}{}_{ik}^{j} u^k, \tag{9}$$

where $\overset{0}{\mathbf{\Gamma}}{}_{i\ k}^{j}$ is known as the Christoffel symbol of the second kind [56], and can be written as [51,54]

$$\overset{0}{\mathbf{\Gamma}}{}_{ik}^{\ j} = \frac{1}{2}\overset{0}{\mathbf{g}}{}^{jl}\left(\frac{\partial\ \overset{0}{g}_{li}}{\partial\ x^{\ k}} + \frac{\partial\ \overset{0}{g}_{lk}}{\partial\ x^{\ i}} - \frac{\partial\ \overset{0}{g}_{ik}}{\partial\ x^{\ l}}\right). \tag{10}$$

It should be pointed out that $\overset{0}{\mathbf{g}}_i$ and $\mathbf{g}_i$ represent two very important local basis vectors; the stretch and rotation of a deformable body are reflected precisely through the transformation of these vectors.

On the other hand, the S-R decomposition theorem [49–54] states that any invertible linear differential transformation function **F** yields a unique additive decomposition:

$$\mathbf{F} = \mathbf{S} + \mathbf{R}, \tag{11}$$

where **S** is a symmetry sub-transformation representing the strain tensor and is positive definite and is called Chen strain, and **R** is an orthogonal sub-transformation representing the local mean rotation tensor.

The strain tensor is

$$S_j^{\ i} = \frac{1}{2}\left(u^i|_j + u^{\ i}|_j^{\mathrm{T}}\right) - L_k^{\ i}L_j^{\ k}(1 - \ \cos\theta), \tag{12}$$

and the rotation tensor is

$$R_j^{\ i} = \delta_j^{\ i} + L_j^{\ i}\sin\theta + L_k^{\ i}L_j^{\ k}(1 - \ \cos\theta), \tag{13}$$

where $L_j^{\ i}$ is the unit vector of the rotation axis, and $u^{\ j}|_i$ is the displacement gradient. The superscript T denotes the transpose, and the notation "$|_{\ i}$" represents the covariant derivative with respect to $\overset{0}{\mathbf{g}}_i$. And $L_j^{\ i}$ can be written as

$$L_j^{\ i} = \frac{1}{2\sin\theta}\left(u^{\ i}|_j - u^{\ i}|_j^{\mathrm{T}}\right). \tag{14}$$

The mean rotation angle θ is determined by the following formula

$$\sin\theta = \frac{1}{2}\sqrt{\left(u^{\ 1}|_2 - u^{\ 1}|_2^{\mathrm{T}}\right)^2 + \left(u^{\ 2}|_3 - u^{\ 2}|_3^{\mathrm{T}}\right)^2 + \left(u^{\ 1}|_3 - u^{\ 1}|_3^{\mathrm{T}}\right)^2}. \tag{15}$$

For two-dimensional problems, Eq. (15) reduces into

$$\sin\theta = \frac{1}{2}\left(u^{\ 1}|_2 - u^{\ 1}|_2^{\mathrm{T}}\right). \tag{16}$$

In addition, the strain rate $\dot{S}_j^{\ i}$ can be written as [51,54]

$$\dot{S}_j^{\ i} = \frac{1}{2}\left(V^{\ i}\|_j + V^{\ i}\|_j^{\mathrm{T}}\right), \tag{17}$$

where $V^{\ i}\|_j$ is the velocity gradient, and the notation "$\|_{\ i}$" represents the covariant derivative with respect to $\mathbf{g}_i$, in order to distinguish it from "$|_{\ i}$". It should be noted that, in accordance with the theory of tensor analysis, the corresponding physical components should be adopted in the calculation.

3. DDA based on S-R decomposition

3.1. Incremental governing equation

Based on the S-R decomposition, the principle of virtual power can be applied to establish the incremental governing equation, with respect to the current configuration. Assuming that the solutions for the static and kinematic variables have been obtained from time 0 up to time t inclusively, and that the subsequent solution for time $t+\Delta t$ is now targeted. The procedure to obtain the solution for the next required equilibrium position is representative, and can be carried out repetitively until the final state is achieved. At time $t+\Delta t$, the principle of virtual power for the deformable body can be expressed by the following equation with respect to the current configuration

$$\int_{t+\Delta t_{\Omega}} {}^{t+\Delta t}\sigma_j{}^i \delta\left({}^{t+\Delta t}\dot{S}_i^j\right) d\Omega + {}^{t+\Delta t}W_{\text{ine}} + {}^{t+\Delta t}W_{\text{pen}} - {}^{t+\Delta t}W_{\text{ext}} = 0, \tag{18}$$

where the first term represents the virtual power corresponding to the inner force, and ${}^{t+\Delta t}W_{\text{ine}}$, ${}^{t+\Delta t}W_{\text{pen}}$ and ${}^{t+\Delta t}W_{\text{ext}}$ are the virtual powers of inertia force, constraint force of specified displacement, and the surface and body force, respectively. Ω is the domain of integration. In addition, $\sigma_j{}^i$ is the stress, and $\delta\dot{S}_i^j$ is the virtual strain rate, with the definitions,

$$ {}^{t+\Delta t}W_{\text{ine}} = {}^{t+\Delta t}\left(\int_{\Omega} \rho A^i \delta V_i d\Omega\right), \tag{19}$$

$$ {}^{t+\Delta t}W_{\text{pen}} = {}^{t+\Delta t}\left(\int_{\Gamma_u} k^i (\Delta u^i - \Delta\breve{u}^i)\delta V_i dS\right), \tag{20}$$

and

$$ {}^{t+\Delta t}W_{\text{ext}} = {}^{t+\Delta t}\left(\int_{\Gamma_P} \breve{P}_i \delta V^i dS + \int_{\Omega} \rho f_i \delta V^i d\Omega\right), \tag{21}$$

where ρ is the material density, A^i is the acceleration, δV^i is the virtual velocity, and k^i is the penalty number; Δu^i and $\Delta\breve{u}^i$ represent the undetermined and specified displacement increments, respectively; $\breve{P}^i$ is the specified traction, and f^i is the force per unit volume. Throughout this paper, the superscript $t+\Delta t$ implies that the representation refers to the configuration of time $t+\Delta t$. It should be noted that Eq. (18) is now specified with respect to the co-moving coordinate system ${}^{t+\Delta t}\mathbf{g}_i$.

In the incremental interval Δt between time t and time $t+\Delta t$, we take

$$ {}^{t+\Delta t}\sigma_j{}^i = {}^t\sigma_j{}^i + \Delta\sigma_j{}^i, \tag{22}$$

and

$$ {}^{t+\Delta t}\dot{S}_j{}^i = {}^t\dot{S}_j{}^i + \Delta\dot{S}_j{}^i, \tag{23}$$

and

$$ {}^{t+\Delta t}V = {}^tV + \Delta V, \tag{24}$$

where $\Delta\sigma_j{}^i$,$\Delta\dot{S}_j{}^i$ and ΔV are the undetermined stress increment, strain rate increment and velocity increment, respectively. Linearizing the stress increment yields

$$\Delta\sigma_j{}^i = \Delta t\dot{\sigma}_j{}^i, \tag{25}$$

where $\dot{\sigma}_j{}^i$ is the unknown stress rate in the incremental interval Δt. Thus, Eq. (22) becomes

$$ {}^{t+\Delta t}\sigma_j{}^i = {}^t\sigma_j{}^i + \Delta t\dot{\sigma}_j{}^i. \tag{26}$$

For time $t+\Delta t$, the values of all variables have been known at time t, namely,

$$\delta\left({}^{t+\Delta t}\dot{S}_j{}^i\right) = \delta\left(\Delta\dot{S}_j{}^i\right), \tag{27}$$

and

$$\delta({}^{t+\Delta t}V) = \delta(\Delta V). \tag{28}$$

In this study, ρ, k^i, and f^i are all treated as constant. At an arbitrary time, the specified stress and displacement boundary conditions might be known; however, the configuration of time $t+\Delta t$ is unknown. Therefore, the following approximation can be employed, and using Eq. (28) gives

$$ {}^{t+\Delta t}W_{\text{pen}} \approx {}^tW_{\text{pen}} = \int_{\Gamma_u} k^i(\Delta u^i - {}^t\Delta\breve{u}^i)\delta(\Delta V^i)dS. \tag{29}$$

In the same fashion, we have

$$ {}^{t+\Delta t}W_{\text{ext}} \approx {}^tW_{\text{ext}} = \int_{\Gamma_P} {}^t\breve{P}_i\delta(\Delta V^i)dS + \int_{{}^t\Omega} \rho f^i\delta(\Delta V^i)d\Omega, \tag{30}$$

and ${}^{t+\Delta t}W_{\text{ine}}$ becomes

$$ {}^{t+\Delta t}W_{\text{ine}} = \int_{t+\Delta t_{\Omega}} \rho\, {}^{t+\Delta t}A_i \delta(\Delta V^i)d\Omega. \tag{31}$$

Substituting Eqs. (26) and (27) into Eq. (28) and considering Eqs. (29), (30) and (31), one can obtain

$$\int_{{}^t\Omega} {}^t\sigma_j^i\delta\left(\Delta\dot{S}_i^j\right)d\Omega + \Delta t\int_{{}^t\Omega} \dot{\sigma}_j^i\delta\left(\Delta\dot{S}_i^j\right)d\Omega + {}^{t+\Delta t}W_{\text{ine}} + {}^tW_{\text{pen}} - {}^tW_{\text{ext}} = 0. \tag{32}$$

This is the so-called the incremental governing equation, where the superscript t means that the description is with respect to the configuration of time t. And Eq. (32) indicates that the virtual work equation Eq. (18) with respect to the configuration of time $t+\Delta t$ has been transformed to that refer to the configuration of time t. $\Delta\dot{S}_i^j$ and ${}^{t+\Delta t}W_{\text{ine}}$ are the undetermined variables and will be disposed next.

3.2. Updated co-moving coordinate formulation

In order to establish the updated co-moving coordinate formulation of the incremental governing equation, the initial co-moving system $\overset{t\,0}{\mathbf{g}}_i$[52] of time t is chosen as the reference frame of the co-moving coordinate system ${}^t\mathbf{g}_i$ at time t. There are three the main purposes of this choice:

(1) Transforming Eq. (32) into an equation with regard to the initial co-moving system $\overset{t\,0}{\mathbf{g}}_i$ at time t.

By using the results of the fourth section in [52], the first two terms (FTT) of Eq. (32) can be written as

$$\text{FTT} = \int_{{}^t\Omega} \bar{\sigma}_j^i\delta\left(\Delta\bar{\dot{S}}_i^j\right)d\Omega + \Delta t\int_{{}^t\Omega} \bar{D}_j{}^i{}_l{}^k\, {}^t\bar{\dot{S}}_k{}^l\,\delta\left(\Delta\bar{\dot{S}}_i^j\right)d\Omega, \tag{33}$$

where $\bar{D}_j{}^i{}_k{}^l$ and $\Delta\bar{\dot{S}}_k{}^l$ are the material tensor and the unknown strain rate increment in the interval Δt with respect to $\overset{t\,0}{\mathbf{g}}_i$, respectively. The bar "−" over a variable indicates that the variable refers to $\overset{t\,0}{\mathbf{g}}_i$.

For time t, the velocity vector referring to the co-moving coordinate systems ${}^t\mathbf{g}_i$ and $\overset{t\,0}{\mathbf{g}}_i$ can be expressed as

$$ {}^t\mathbf{V} = {}^tV_i\, {}_t\mathbf{g}_i = \bar{V}^i\, {}^t\overset{0}{\mathbf{g}}_i. \tag{34}$$

Similarly, the velocity increment vector is given as

$$\Delta^t\mathbf{V} = \Delta^tV_i\, {}_t\mathbf{g}_i = \Delta\bar{V}^i\, {}^t\overset{0}{\mathbf{g}}_i. \tag{35}$$

For time $t+\Delta t$, with respect to the co-moving coordinate systems ${}^{t+\Delta t}\mathbf{g}_i$ and $\overset{t+\Delta t\,0}{\mathbf{g}}_i$, which is the initial co-moving system of ${}^{t+\Delta t}\mathbf{g}_i$, we can obtain

$$\Delta^{t+\Delta t}\mathbf{V} = \Delta^{t+\Delta t}V_i\, {}_{t+\Delta t}\mathbf{g}_i = \Delta\bar{\bar{V}}^i\, {}^{t+\Delta t}\overset{0}{\mathbf{g}}_i, \tag{36}$$

where the double bar "=" over a variable indicates that the variable refers to $\overset{t+\Delta t\,0}{\mathbf{g}}_i$ in order to distinguish with the variable referring to $\overset{t\,0}{\mathbf{g}}_i$. At time $t+\Delta t$, on the other hand, the acceleration vector [51,54] can be defined by

$$\mathbf{A} = {}^{t+\Delta t}A^{i}\,{}^{t+\Delta t}\mathbf{g}_i = {}^{t+\Delta t}\left(\frac{\partial V^i}{\partial t} + V^j V^i\|_j\right){}^{t+\Delta t}\mathbf{g}_i. \tag{37}$$

As for the first term of Eq. (37), owing to fact that the space derivative is not involved, we have

$${}^{t+\Delta t}\left(\frac{\partial V^i}{\partial t}\right){}^{t+\Delta t}\mathbf{g}_i = \left(\frac{\partial \overline{V}^i}{\partial t}\right){}^{t+\Delta t}\overset{0}{\mathbf{g}}_i. \tag{38}$$

Furthermore, for the second term of Eq. (37), using the following two equations [52]

$${}^{t+\Delta t}\mathbf{g}_i = \left(\frac{\partial\,{}^{t+\Delta t}x^j}{\partial x^i}\right){}^{t+\Delta t}\overset{0}{\mathbf{g}}_i, \tag{39}$$

$${}^{t+\Delta t}V^i\|_j \frac{\partial\,{}^{t+\Delta t}x^k}{\partial x^i} = {}^{t+\Delta t}\overline{V}^k|_i \frac{\partial x^i}{\partial x^j}, \tag{40}$$

we have

$$\mathbf{A} = {}^{t+\Delta t}A^i\,{}^{t+\Delta t}\mathbf{g}_i = {}^{t+\Delta t}\left(\frac{\partial V^i}{\partial t} + V^j V^i\|_j\right){}^{t+\Delta t}\mathbf{g}_i$$
$$= \left(\frac{\partial \overline{V}^i}{\partial t} + \overline{V}^j\overline{V}^i|_j\right){}^{t+\Delta t}\overset{0}{\mathbf{g}}_i = \overline{A}^i\,{}^{t+\Delta t}\overset{0}{\mathbf{g}}_i. \tag{41}$$

By using Eqs. (36) and (41), the virtual powers of the inertia force ${}^{t+\Delta t}W_{\mathrm{ine}}$, in reference to ${}^{t+\Delta t}\overset{0}{\mathbf{g}}_i$, can be expressed as

$${}^{t+\Delta t}W_{\mathrm{ine}} = \overline{W}_{\mathrm{ine}} = \int_{{}^{t+\Delta t}\Omega}\rho\left(\frac{\partial \overline{V}^i}{\partial t} + \overline{V}^j\overline{V}^i|_j\right)\delta(\Delta\overline{V}^i)d\Omega. \tag{42}$$

With respect to ${}^{t}\overset{0}{\mathbf{g}}_i$ and ${}^{t+\Delta t}\overset{0}{\mathbf{g}}_i$, the velocity increment vectors can be written as

$$\Delta\mathbf{V} = \Delta\overline{V}^i\,{}^{t}\overset{0}{\mathbf{g}}_i = \Delta\overline{\overline{V}}^i\,{}^{t+\Delta t}\overset{0}{\mathbf{g}}_i. \tag{43}$$

Because ${}^{t}\overset{0}{\mathbf{g}}_i$ and ${}^{t+\Delta t}\overset{0}{\mathbf{g}}_i$ are isomorphic, namely,

$$\Delta\overline{V}^i = \Delta\overline{\overline{V}}^i. \tag{44}$$

Thus, Eq. (42) becomes

$${}^{t+\Delta t}W_{\mathrm{ine}} = \overline{W}_{\mathrm{ine}} = \int_{{}^{t+\Delta t}\Omega}\rho\left(\frac{\partial \overline{V}^i}{\partial t} + \overline{V}^j\overline{V}^i|_j\right)\delta(\Delta\overline{V}^i)d\Omega. \tag{45}$$

Moreover, using Eq. (35) yields

$${}^{t}W_{\mathrm{pen}} = \overline{W}_{\mathrm{pen}} = \int_{\Gamma_u} k^i(\Delta u^i - {}^{t}\Delta\breve{u}^i)\delta(\Delta\overline{V}^i)dS, \tag{46}$$

and

$${}^{t}W_{\mathrm{ext}} = \overline{W}_{\mathrm{ext}} = \int_{\Gamma_P}{}^{t}\breve{P}_i\,\delta(\Delta\overline{V}^i)dS + \int_{\Omega}\rho f^i\delta(\Delta\overline{V}^i)d\Omega, \tag{47}$$

where $\overline{W}_{\mathrm{pen}}$ and $\overline{W}_{\mathrm{ext}}$ are both expressed with respect to the co-moving coordinate system ${}^{t}\overset{0}{\mathbf{g}}_i$. Hence, the incremental governing equation Eq. (32) becomes

$$\int_{{}^{t}\Omega}\overline{\sigma}^i_j\,\delta(\Delta\overline{S}^j_i)d\Omega + \Delta t\int_{{}^{t}\Omega}\overline{D}^i_j{}^k_l\,\overline{S}^l_k\,\delta\left(\Delta\overline{S}^j_i\right)d\Omega + \overline{W}_{\mathrm{ine}} + \overline{W}_{\mathrm{pen}} - \overline{W}_{\mathrm{ext}} = 0. \tag{48}$$

Eqs. (45–48) exactly express the new formulation, which is based on the S-R decomposition theorem and is described in the updated co-

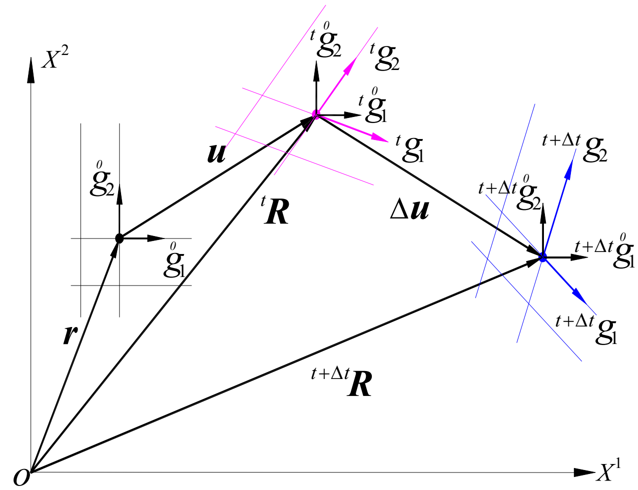

Fig. 2. Update of the co-moving coordinate.

moving coordinate form. The equations will be implemented further in the context of DDA. It should be pointed out that the rotation tensor **R** does not appear explicitly, and that the inertia item is primarily considered. The above two points are the main differences from the counterpart employed [52]. Moreover, a dynamic analysis cannot be achieved despite the insertion of the inertia item into the static formulation [52]. That is, there seems to be no shortcut to the dynamic formulation.

(2) Providing theoretical basis for updating the co-moving coordinate and state variables of material point.

In solving the incremental governing equation, the initial co-moving system of each incremental step is required to be reselected and constantly changing. That is, from time t to time $t+\Delta t$, the initial co-moving system is given by ${}^{t}\overset{0}{\mathbf{g}}_i$ at time t; whereas, from time $t+\Delta t$ to time $t+\Delta t+\Delta t$, the initial co-moving system is defined by ${}^{t+\Delta t}\overset{0}{\mathbf{g}}_i$ at time $t+\Delta t$, as shown in Fig. 2. For the case that these initial co-moving systems are all selected to be isomorphic to the rectilinear orthogonal coordinate system that is fixed in the space, a formula for updating the co-moving coordinate of material point has been given by [52]:

$${}^{t+\Delta t}x^i = {}^{t}x^i + \Delta\overset{0}{u}{}^i, \tag{49}$$

where $\Delta\overset{0}{u}{}^i$ is the displacement increment in the ${}^{t}\overset{0}{\mathbf{g}}_i$ system during Δt. As for the stress, the following formula can be adopted:

$${}^{t+\Delta t}\overline{\sigma}^i_j = {}^{t}\overline{\sigma}^i_j + \Delta t\dot{\overline{\sigma}}^i_j = {}^{t}\overline{\sigma}^i_j + \Delta t\,\overline{D}^i_j{}^k_l\,\Delta\overline{S}^l_k. \tag{50}$$

It is worth mentioning that $\dot{\overline{\sigma}}^i_j$ is also an objective stress rate in the ${}^{t}\overset{0}{\mathbf{g}}_i$ system. For an isotropic material, $\overline{D}^i_j{}^l_k = D^i_j{}^l_k$ was proved in [52].

(3) Due to the above-mentioned property, when isomorphic coordinate systems are chosen, the Christoffel symbol of the second kind, $\overset{0}{\boldsymbol{\Gamma}}{}^j_{ik}$, will vanish from Eq. (9). The covariant derivative $u^j|_i$ becomes

$$u^j|_i = \frac{\partial u^j}{\partial x^i}. \tag{51}$$

Therefore, the related deduction and calculation can be simplified considerably. From here on, $\overset{0}{\boldsymbol{\Gamma}}{}^j_{ik}$ will no longer be required, unless otherwise noted.

3.3. Governing equation and time advancement

Now we start to construct SRDDA$_{vp}$. In order to facilitate the description, the bar "−" and the double bar "=" over some variables are omitted from this point on, unless otherwise noted. The first-order displacement approximation is adopted for any block. In this study, the following shape function is used

$$\mathbf{T}(x,y)=\begin{bmatrix}1 & 0 & y_0-y & x-x_0 & 0 & \frac{y-y_0}{2}\\ 0 & 1 & x-x_0 & 0 & y-y_0 & \frac{x-x_0}{2}\end{bmatrix}. \tag{52}$$

Considering an arbitrary shape block B, for any point (x, y) inside the block B, the displacement $\mathbf{u}$ can be expressed as

$$\mathbf{u}(x,y)=\begin{pmatrix}u^{x}(x,y)\\ u^{y}(x,y)\end{pmatrix}=\mathbf{T}(x,y)\mathbf{d}_b, \tag{53}$$

where $\mathbf{d}_b=\{u,v,\theta,\varepsilon_x,\varepsilon_y,\gamma_{xy}\}^{\mathrm{T}}$is the generalized displacement vector of the block. u and v represent translational components of the block. While θ is corresponding to the mean rotation angle in S-R decomposition theorem. ε_x, ε_y and γ_{xy} are the three Cauchy strain components. Further, the increment displacement $\Delta\mathbf{u}$ can be described as

$$\Delta\mathbf{u}(x,y)=\begin{pmatrix}\Delta u^{x}(x,y)\\ \Delta u^{y}(x,y)\end{pmatrix}=\mathbf{T}(x,y)\Delta\mathbf{d}_b, \tag{54}$$

where $\Delta\mathbf{d}_b=\{\Delta u,\Delta v,\Delta\theta,\Delta\varepsilon_x,\Delta\varepsilon_y,\Delta\gamma_{xy}\}^{\mathrm{T}}$is the generalized increment displacement vector of the block. The velocity $\mathbf{V}$ can be written as

$$\mathbf{V}(x,y)=\begin{pmatrix}v^{x}(x,y)\\ v^{y}(x,y)\end{pmatrix}=\mathbf{T}(x,y)\mathbf{V}_b, \tag{55}$$

where $\mathbf{V}_b=\{\dot u,\dot v,\dot\theta,\dot\varepsilon_x,\dot\varepsilon_y,\dot\gamma_{xy}\}^{\mathrm{T}}$is the generalized velocity vector of the block. Moreover, the acceleration $\mathbf{A}$ can be expressed as

$$\mathbf{A}(x,y)=\begin{pmatrix}A^{x}(x,y)\\ A^{y}(x,y)\end{pmatrix}=\mathbf{T}(x,y)\mathbf{A}_b. \tag{56}$$

where $\mathbf{A}_b=\{\ddot u,\ddot v,\ddot\theta,\ddot\varepsilon_x,\ddot\varepsilon_y,\ddot\gamma_{xy}\}^{\mathrm{T}}$is the generalized acceleration vector of the block. On the other hand, to represent the stress and strain of any point inside of the block, the vectors $\boldsymbol{\sigma}(x,y)=\{\sigma_1^1,\sigma_2^2,\sigma_2^1\}^{\mathrm{T}}$ and $\mathbf{S}(x,y)=\{S_1^1,S_2^2,2S_2^1\}^{\mathrm{T}}$(refer to Eq. (12)) can be employed, respectively. The strain rate vector of any point can be expressed as (refer to Eq. (17))

$$\dot{\mathbf{S}}(x,y)=\left\{\dot S_1^1,\dot S_2^2,2\dot S_2^1\right\}=\mathbf{B}_b\mathbf{V}_b, \tag{57}$$

where

$$\mathbf{B}_b=\begin{bmatrix}0&0&0&1&0&0\\0&0&0&0&1&0\\0&0&0&0&0&1\end{bmatrix}, \tag{58}$$

and the strain rate increment vector can be written as

$$\Delta\dot{\mathbf{S}}(x,y)=\left\{\Delta\dot S_1^1,\Delta\dot S_2^2,2\Delta\dot S_2^1\right\}=\mathbf{B}_b\Delta\mathbf{V}_b. \tag{59}$$

Noticing the arbitrariness of $\delta(\Delta\mathbf{V}_b)$, Eq. (48) can be recast in the following matrix format

$$\int_\Omega \mathbf{B}_b^{\mathrm{T}}\boldsymbol{\sigma}d\Omega+\Delta t\int_\Omega \mathbf{B}_b^{\mathrm{T}}\mathbf{D}\,\mathbf{B}_b\mathbf{V}_b\,d\Omega+\underbrace{\int_\Omega \rho\mathbf{T}^{\mathrm{T}}\mathbf{T}\,\mathbf{A}_b d\Omega}_{\text{Dynamic terms}}+\mathbf{W}_{\mathrm{pen}}-\mathbf{W}_{\mathrm{ext}}=0, \tag{60}$$

where $\mathbf{D}$ is the material matrix, and

$$\mathbf{W}_{\mathrm{pen}}=\int_{\Gamma_u}\mathbf{T}^{\mathrm{T}}\mathbf{k}(\mathbf{T}\Delta\mathbf{d}_b-\Delta\breve{\mathbf{u}})dS, \tag{61}$$

$$\mathbf{W}_{\mathrm{ext}}=\int_{\Gamma_P}\mathbf{T}^{\mathrm{T}}\breve{\mathbf{P}}dS+\int_\Omega \rho\mathbf{T}^{\mathrm{T}}\mathbf{f}\,d\Omega, \tag{62}$$

where $\Delta\breve{\mathbf{u}}$, $\breve{\mathbf{P}}$ and $\mathbf{f}$ are the specified increment displacement, specified traction, and force per unit volume, respectively. The penalty matrix $\mathbf{k}$ is

$$\mathbf{k}=\begin{bmatrix}k^{x} & 0\\ 0 & k^{y}\end{bmatrix}. \tag{63}$$

It should be noted that the definitions of the stress and the velocity [54] must be employed, with respect to the co-moving coordinate system. Next, the disposition of the dynamic terms in Eq. (60) will be explained based on the generalized-α method [55], which is an implicit method for dynamic analysis. The velocities and accelerations of the Newmark format [57] at the end of time $t+\Delta t$ are as follows:

$$^{t+\Delta t}\mathbf{V}_b=\frac{\gamma}{\beta\,\Delta t}\Delta\mathbf{d}_b-\frac{\gamma-\beta}{\beta}{}^{t}\mathbf{V}_b-\frac{\gamma-2\beta}{2\beta}\Delta t\;{}^{t}\mathbf{A}_b, \tag{64}$$

$$^{t+\Delta t}\mathbf{A}_b=\frac{1}{\beta(\Delta t)^2}\Delta\mathbf{d}_b-\frac{1}{\beta\,\Delta t}{}^{t}\mathbf{V}_b-\frac{1-2\beta}{2\beta}{}^{t}\mathbf{A}_b. \tag{65}$$

The generalized mid-point velocities and accelerations are given by [55]

$$^{t+\Delta t-\alpha_f}\mathbf{V}_b=\frac{(1-\alpha_f)\gamma}{\beta\,\Delta t}\Delta\mathbf{d}_b-\frac{(1-\alpha_f)\gamma-\beta}{\beta}{}^{t}\mathbf{V}_b-\frac{(1-\alpha_f)(\gamma-2\beta)}{2\beta}\Delta t\;{}^{t}\mathbf{A}_b, \tag{66}$$

$$^{t+\Delta t-\alpha_m}\mathbf{A}_b=\frac{1-\alpha_m}{\beta(\Delta t)^2}\Delta\mathbf{d}_b-\frac{1-\alpha_m}{\beta\,\Delta t}{}^{t}\mathbf{V}_b-\frac{1-\alpha_m-2\beta}{2\beta}{}^{t}\mathbf{A}_b, \tag{67}$$

where β, γ, α_f and α_m are the algorithmic parameters and the relationship between them are as follows:

$$\beta=\frac{1}{4}(1-\alpha_m+\alpha_f)^2,\quad \gamma=\frac{1}{2}-\alpha_m+\alpha_f, \tag{68}$$

where

$$\alpha_m=\frac{2\rho_\infty-1}{\rho_\infty+1},\quad \alpha_f=\frac{\rho_\infty}{\rho_\infty+1}, \tag{69}$$

and ρ_∞ denotes the spectral radius.

After some mathematical manipulations, the incremental governing equation of one block can be written as

$$(\mathbf{K}_b+\mathbf{M}_b)\Delta\mathbf{d}_b=\mathbf{F}_b, \tag{70}$$

where $\mathbf{K}_b$, $\mathbf{M}_b$ and $\mathbf{F}_b$ are the stiffness matrix, the mass matrix and the equivalent force vector of the block, respectively. As for the other matrices, such as matrices of normal contact and shear contact and friction force, they are similar to those given by [1]. Once these matrices are obtained, the global control equation can easily be assembled. Up to now, SRDDA$_{vp}$ is established.

It should be pointed out that SRDDA$_{vp}$ possesses the ability to capture the deformation and rotation simultaneously, which inherits from the S-R decomposition theorem. Exactly due to this ability, SRDDA can naturally eliminate the volume expansion of blocks.

4. Numerical examples

In this section, several classical tests are analyzed to validate the availability and potential of SRDDA$_{vp}$. In this study, DDA^0 signifies the original DDA [1], DDA^1 denotes the enhanced DDA by post-adjustment method [24] to eliminate the volume expansion. It should be pointed out that Eigen [58], which is a C++ template library for linear algebra, is used to solve the governing equation.

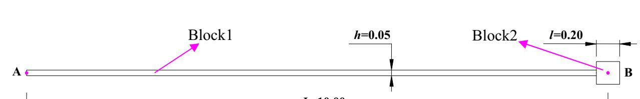

Fig. 3. Configuration of a simple pendulum.

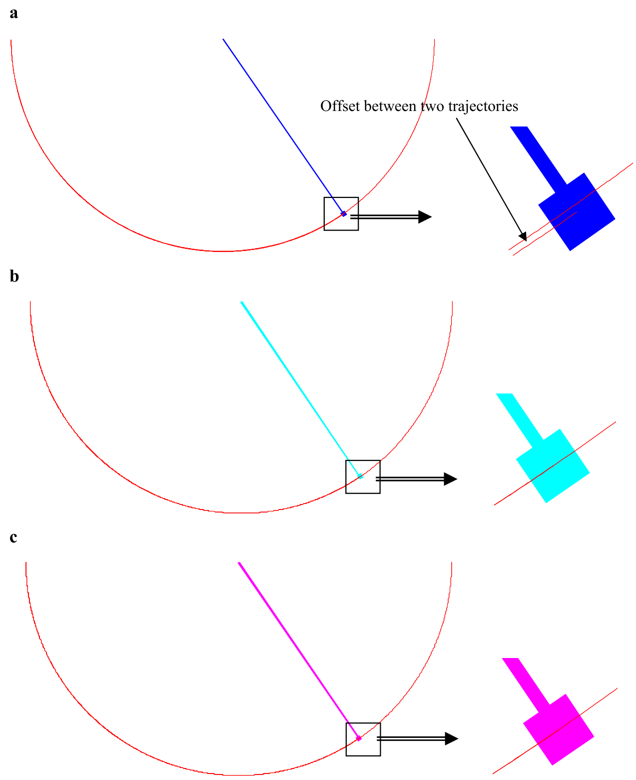

Fig. 4. Trajectories of point B given by: (a) DDA^0; (b) DDA^1 and (c) SRDDA$_{vp}$.

Table 1
Area of Block1 and Block2 (Fig. 3).

CS		DDA^0		DDA^1		SRDDA$_{vp}$	
		CV	RE (%)	CV	RE (%)	CV	RE (%)
500	Block1	0.495021	0.0042	0.495000	0.0000	0.495000	0.0000
	Block2	0.040002	0.0042	0.040000	0.0000	0.040000	0.0000
1000	Block1	0.495162	0.0326	0.495000	0.0000	0.495001	0.0001
	Block2	0.040013	0.0326	0.040000	0.0000	0.040000	0.0000
2000	Block1	0.495983	0.1986	0.495000	0.0000	0.495001	0.0002
	Block2	0.040079	0.1986	0.040000	0.0000	0.040000	0.0000
5000	Block1	0.497018	0.4077	0.495000	0.0000	0.495001	0.0001
	Block2	0.040163	0.4077	0.040000	0.0000	0.040001	0.0002
6000	Block1	0.497932	0.5924	0.495000	0.0000	0.495001	0.0002
	Block2	0.040237	0.5924	0.040000	0.0000	0.040000	0.0000

Analytical solution: $Area1 = 0.495\ \text{m}^2$, $Area2 = 0.04\ \text{m}^2$. (CS: calculation step, CV: calculation value, RE: relative error)

Table 2
Maximum angular velocity of a simple pendulum (Fig. 3).

Direction of motion	Method	CV	RE (%)
Left-to-right	DDA^0	−1.413895	−0.0226
	DDA^1	−1.415474	0.0891
	SRDDA$_{vp}$	−1.415475	0.0892
Right-to-left	DDA^0	1.413342	−0.0617
	DDA^1	1.418137	0.2774
	SRDDA$_{vp}$	1.416118	0.1346

Analytical solution: $\omega = \mp 1.414214\ \text{s}^{-1}$.(CV: calculation value, RE: relative error)

4.1. Simple pendulum

In Fig. 3, Block1 is a long rod with a length of 9.90 m and a high of h=0.05 m; Block2 is a quadrate and its length of side is l=0.20 m. Point A serves as the center of rotation, point B is the centroid of Block2, and the distance between points A and B is given by L=10.00 m. Block1 and Block2 are connected at point B by contact springs with a stiffness of 0.20×10^{11} MN/m.

The simple pendulum falls from a horizontal position. In this example, the gravity of Block2 is the only external force and the mass of the Block1 is not considered. Let the time step size $\boldsymbol{\Delta}$=0.001 s, the acceleration of gravity g =−10 m/s^2, Young's modulus E =0.20×10^{11} MPa, Poisson's ratio υ=0.25, the penalty parameter P=0.20×10^{11} MPa, and the spectral radius of the generalized-α method [55] $\rho_\infty = 1$. The total number of calculation steps is 6000, and the open-close iterations are not performed during the simulation. The trajectories of point B are shown in Fig. 4, and the some data are listed in Tables 1, 2.

From the zoomed view in Fig. 4(a), there is an offset between two trajectories, which are corresponding to the two different directions of motion. This is because the false volume expansion is not removed in DDA^0. While in Fig. 4(b) and (c), the offsets of trajectories are not observed, implying that the false volume expansion is overcome effectively by DDA^1 and SRDDA$_{vp}$. The effectiveness of SRDDA$_{vp}$ is proved further by the data in Table 1. It should be emphasized that compared with DDA^1, the accuracy of the maximum angular velocity of the simple pendulum is improved obviously by SRDDA$_{vp}$ (see Table 2), especially for the motion from right to left. The relative error is reduced to RE=0.1346% from RE=0.2774%, implying that the maximum angular velocity given by SRDDA$_{vp}$ is closer to the theoretical solution.

4.2. Swing of a slender rod

The configuration of a slender rod is shown in Fig. 5. The length and high of the rod are L=10.00 m, h=0.10 m, respectively. Point A is the center of rotation, and point B is the centroid of rod. The slender rod falls freely from a horizontal position. Let the time step size $\boldsymbol{\Delta}$=0.001 s, the acceleration of gravity g =−10 m/s^2, Young's modulus E =0.20×10^{11} MPa, Poisson's ratio υ=0.25, the penalty parameter P=0.20×10^{11} MN/m. And the spectral radius of the generalized-α method [55] $\rho_\infty = 1$. Under the action of gravity the slender rod starts fall from a horizontal position. The total number of calculation steps is 5000. The trajectories of points B and C are shown in Fig. 6, and the some data are listed in Tables 3 and 4.

From the zoomed view in Fig. 6(a), there is also an offset between two trajectories; this is also caused by the false volume expansion. From Table 3, as we can see, the false volume expansion basically does not exist in DDA^1 and SRDDA$_{vp}$. Moreover, from Table 4, the accuracy of maximum angular velocity of the slender rod is enhanced significantly by SRDDA$_{vp}$, especially for the movement from right to left. The relative error is reduced to RE=0.1608% from RE=0.2834%. It would be more meaningful for long time simulation.

4.3. Propagation of a sine wave

Now, the propagation of a sine wave is used to verify SRDDA$_{vp}$. A bar-spring structure (Fig. 7) serves as the medium. The bar-spring structure consists of 40 bars and 39 springs. For each bar, the length is given by l=0.25 m and the height is h=0.10 m, respectively. The distance is L=10.00 m between points A and B. Let the time step length $\boldsymbol{\Delta}$=0.005 s, Young's modulus E =0.20×10^{5} MPa, Poisson's ratio

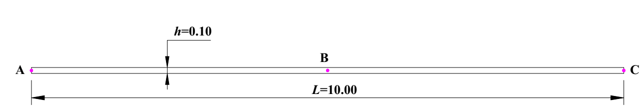

Fig. 5. Configuration of a slender rod.

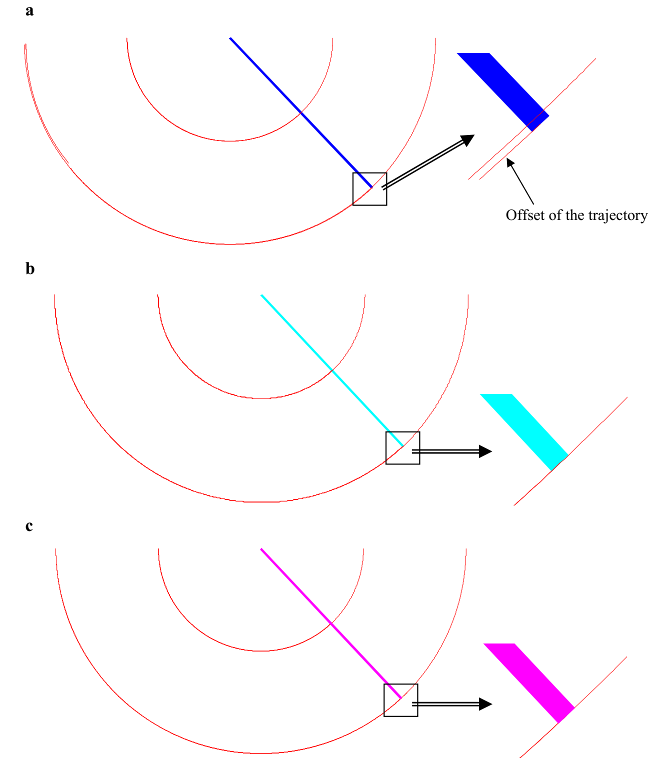

Fig. 6. Trajectories of points B and C given by: (a) DDA^0; (b) DDA^1 and (c) $SRDDA_{vp}$.

Table 3
Area of a slender rod (Fig. 5).

CS	DDA^0		DDA^1		$SRDDA_{vp}$	
	CV	RE (%)	CV	RE (%)	CV	RE (%)
500	1.000093	0.0093	1.000000	0.0000	1.000001	0.0001
1000	1.000716	0.0716	1.000000	0.0000	1.000002	0.0002
2000	1.003383	0.3383	1.000000	0.0000	1.000002	0.0002
5000	1.007500	0.7500	1.000000	0.0000	1.000002	0.0002

Analytical solution: $Area = 1.00\ \mathrm{m}^2$. (CS: calculation step, CV: calculation value, RE: relative error)

Table 4
Maximum angular velocity of a slender rod (Fig. 5).

Direction of motion	Method	CV	RE (%)
Left-to-right	DDA^0	−1.731942	−0.0063
	DDA^1	−1.733668	0.0934
	$SRDDA_{vp}$	−1.732869	0.0472
Right-to-left	DDA^0	1.731777	−0.0158
	DDA^1	1.736959	0.2834
	$SRDDA_{vp}$	1.734837	0.1608

Analytical solution: $\omega = \pm 1.732051\ \mathrm{s}^{-1}$. (CV: calculation value, RE: relative error)

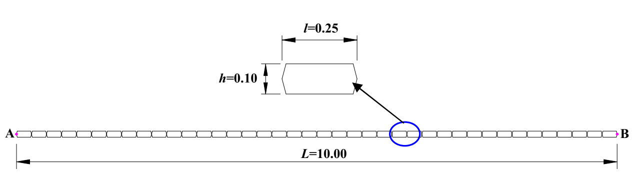

Fig. 7. Configuration of a bar-spring structure.

υ=0.25, the stiffness of springs k=200 MN/m, the penalty parameter P=200 MN/m, and the spectral radius of the generalized-α method [55] $\rho_\infty = 1$. The total number of calculation steps is 900. Moreover, the

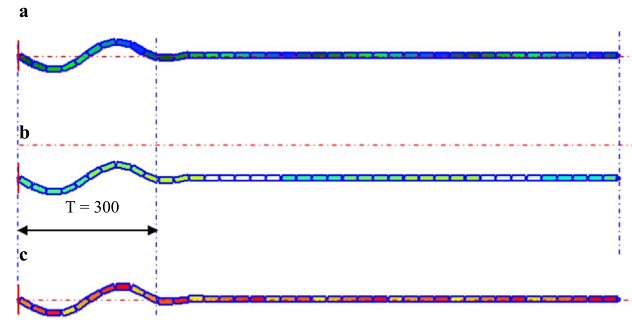

Fig. 8. One period of a sine wave given by: (a) DDA^0; (b) DDA^1 and (c) $SRDDA_{vp}$.

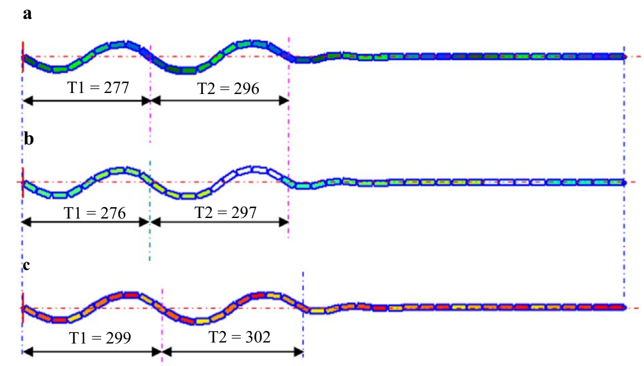

Fig. 9. Two periods of a sine wave given by: (a) DDA^0; (b) DDA^1 and (c) $SRDDA_{vp}$.

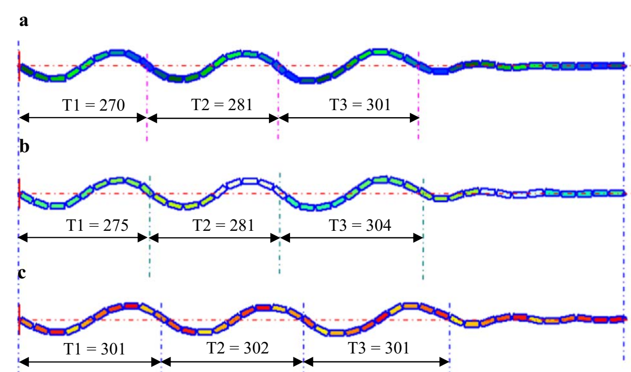

Fig. 10. Three periods of a sine wave given by: (a) DDA^0; (b) DDA^1 and (c) $SRDDA_{vp}$.

weights of bars are ignored and point B is always fixed in the horizontal direction during simulation. The following displacement is assigned to point A.

$$u = 0$$
$$v = 0.25 \sin\left(\frac{2\pi}{300} n\right), \tag{71}$$

where n is the current calculation step. Eq. (71) indicates that the amplitude A =0.25 and the period T=300 CS of the sine wave. Some results are shown in Figs. 8–10.

At CS =300, see Fig. 8, DDA^0, DDA^1 and $SRDDA_{vp}$ all can obtain the accurate period T=300 CS; while at CS =600, see Fig. 9, only $SRDDA_{vp}$ can give the accurate period, namely, T1=299 CS for the first period and T2=302 CS for the second period. For DDA^0 and DDA^1, the total number of calculation steps corresponding to two periods is shortened to about 573 CS. At CS =900, see Fig. 10, the distinction becomes clearer between the periods given by DDA^0, DDA^1 and SRDDA. Especially for the first period, the periods obtained by DDA^0, DDA^1 and $SRDDA_{vp}$ are T1=270 CS, 275 CS and 301 CS, respectively. In general, only for the third period, DDA^0 and DDA^1 can obtain the acceptable period T3=301 CS and 304 CS, respectively.

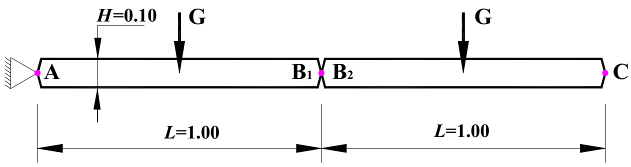

Fig. 11. Configuration of a nunchaku.

While, for the all three periods, $SRDDA_{vp}$ can always give the satisfactory period, namely T1=301 CS, T2=302 CS and T3=301 CS. The shorter period means the faster velocity, thus, the velocity of propagation of the sine wave is increased by DDA^0 and DDA^1.

4.4. Wiggle of a nunchaku

A nunchaku is consisted of two sticks AB_1 and B_2C, and for each stick the length is L =1.00 m and the high is h =0.10 m, respectively, as shown in Fig. 11. Point A is always fixed in double directions and the stiffness of fixed springs is given by k=0.20×10^{15} N/m. Points B_1, B_2 and C are chosen as the three checking points. Moreover, Young's modulus E =0.20×10^{11} Pa, Poisson's ratio υ =0.45, the density of material ρ =2500 kg/m^3, and the acceleration of gravity g =−10 m/s^2, and the spectral radius of the generalized-α method [55] $\rho_\infty = 1$. Let the time step length to be $\mathbf{\Delta}$=0.002 s, and the total calculation step is 1800. Under the action of gravity the nunchaku falls from a horizontal position.

In this example, during the course of the simulation, we want to achieve a scenario that points B_1 and B_2 are always coincide with each other at any instant. Namely, there is the following constrain between points B_1 and B_2 at each calculation step.

$$\begin{pmatrix}\Delta u_{B_1}^x\\ \Delta u_{B_1}^y\end{pmatrix}-\begin{pmatrix}\Delta u_{B_2}^x\\ \Delta u_{B_2}^y\end{pmatrix}=\mathbf{T}_{AB_1}(x_{B_1},y_{B_1})\Delta\mathbf{d}_{AB_1}-\mathbf{T}_{B_2C}(x_{B_2},y_{B_2})\Delta\mathbf{d}_{B_2C}=\begin{pmatrix}0\\0\end{pmatrix},\tag{72}$$

where $(\Delta u_{B_1}^x,\ \Delta u_{B_1}^y)$ and $(\Delta u_{B_2}^x,\ \Delta u_{B_2}^y)$ the increment displacements of points B_1 and B_2, respectively. And $\Delta\mathbf{d}_{AB_1}$ and $\Delta\mathbf{d}_{B_2C}$ are the generalized displacement vectors of the sticks AB_1 and B_1C, respectively. Additionally, $\mathbf{T}_{AB_1}(x_{B_1},y_{B_1})$ and $\mathbf{T}_{B_2C}(x_{B_2},y_{B_2})$ are the shape functions corresponding to the sticks AB_1 and B_1C, respectively (refer to Eq. (52)). Introduction of the Lagrange multipliers λ_1 and λ_2 yields

$$\begin{bmatrix}\mathbf{A}_{12\times12} & \tilde{\mathbf{T}}^{T}_{12\times2}\\ \tilde{\mathbf{T}}_{2\times12} & \mathbf{0}_{2\times2}\end{bmatrix}\begin{bmatrix}\Delta\tilde{\mathbf{d}}_{12\times1}\\ \boldsymbol{\lambda}_{2\times1}\end{bmatrix}=\begin{bmatrix}\tilde{\mathbf{F}}_{12\times1}\\ \mathbf{0}_{2\times1}\end{bmatrix},\tag{73}$$

where

$$\tilde{\mathbf{T}}=[\mathbf{T}_{AB_1},\ \ -\mathbf{T}_{B_2C}],\quad \boldsymbol{\lambda}=[\lambda_1,\ \ \lambda_2]^{T},\tag{74}$$

and

$$\Delta\tilde{\mathbf{d}}=\begin{bmatrix}\Delta\mathbf{d}_{AB_1}\\ \Delta\mathbf{d}_{B_2C}\end{bmatrix},\tag{75}$$

As for the matrixes $\mathbf{A}_{12\times12}$ and $\tilde{\mathbf{F}}_{12\times1}$ one can be refer to Eq. (70). Some results are shown in Fig. 12.

From the zoomed view in Fig. 12(a), it is apparent that the trajectories of points B_1 (the blue solid line) and B_2 (the red solid line) are coincidence; while there is an offset between two trajectories corresponding to the to-and-fro movement of the nunchaku. Now, let us see Fig. 12(b), for point B_1 there is not an offset; however, the trajectories of points B_1 (the blue solid line) and B_2 (the red solid line) do not overlap, this phenomenon is against the control equation Eq. (73). On the other hand, in Fig. 12(c) it cannot be observed that the separation and offset associated with points B_1 and B_2.

The some distances between points B_1 and B_2 obtained by DDA^0, DDA^1 and $SRDDA_{vp}$ are list in Table 5.

From Table 5, as we can see, for DDA^0 and $SRDDA_{vp}$ the distance between points B_1 and B_2 are always equal to zero, this fully complies with the governing equation Eq. (73). However, for DDA^1 the distance is lengthening gradually even though that the angular velocity of the nunchaku is fluctuant and completely regardless of the constraint of Lagrange multipliers on them.

Fig. 13 shows further the trajectories of point C obtained by DDA^0, DDA^1 and $SRDDA_{vp}$. The difference between them is easily observed.

4.5. Simulation of rockfall

A model test example, which is to be conducted, is designed to demonstrate the capability of $SRDDA_{vp}$ to treat large rotation. The model configuration is shown in Fig. 14. On a portion of a rocky slope, a stone, with an initial velocity $\boldsymbol{V}_0$=(2.50 m/s, 0)and angular velocity ω_0 = -1.00 s^{-1}, is falling under the action of gravity. The first length L_1=1.00 m, the second length L_2=2.00 m, the third length L_3=3.00 m and the forth length L_4=5.00 m. The three slope angles are α = 60°, β = 45° and γ = 15°, respectively.

Points P_3, P_4, and P_5 are fixed in double directions. Points P_1 and P_2 are the centroid and a vertex of the stone, respectively. Let the maximum allowable step displacement ratio to be 0.001, the time step size $\mathbf{\Delta}$=0.0005 s, Young's modulus E =0.10×10^8 MPa, Poisson's ratio υ=0.35, the acceleration of gravity g =−10 m/s^2, the spectral radius of the generalized-α method [55] $\rho_\infty = 1$ and the penalty parameter is 50E. The total calculation step is 4000. Considering the fact that the volume expansion is mainly caused by the large rotation, thus, we will pay more attention to the angular velocity. Some data are listed Tables 6 and 7, while the trajectories of points P_1 and P_2 are shown in Fig. 15.

From Table 6, we conclude that before CS=1382 (see Fig. 15), at which the first contact occurs between the slope and the stone, the angular velocities given by DDA^0 and DDA^1 are nearly equal. By comparison, the angular velocities by $SRDDA_{vp}$ are more accurate. For example, at CS =1000, the relative errors are 0.000203% (DDA^0), 0.000203% (DDA^1) and 0.000040% ($SRDDA_{vp}$), respectively.

At CS =1382, the stone touches the slope for the first time (see Fig. 15). Then, at the following calculation step (CS =1383), the angular velocities by DDA^0, DDA^1 and SRDDA are different, with −10.25734346 s^{-1}, −8.85281450 s^{-1} and −8.85595077 s^{-1}, respectively. Moreover, due to the issue of volume expansion, the second contact by DDA^0 can be observed at CS =1973 (see Fig. 15); while for DDA^1 and $SRDDA_{vp}$, the second contact occurs at CS =2005. Whereafter, the third contact appears at CS =2912, 2593 and 2821 corresponding to DDA^0, DDA^1 and $SRDDA_{vp}$, respectively.

From Table 7, for DDA^1 and $SRDDA_{vp}$, the moments of the second contact (CS =2005) is the same. However, at the next calculation step (CS =2006), the angular velocities by DDA^1 and $SRDDA_{vp}$ are different, namely −18.34628241 s^{-1} and −18.55805717 s^{-1}, respectively. While, following the third contact, namely at CS =2913, 2594 and 2822, respectively. The angular velocities by DDA^0, DDA^1 and $SRDDA_{vp}$ are 2.77335470 s^{-1}, −23.45725286 s^{-1} and 14.49043619 s^{-1}, respectively.

In Fig. 15, the blue line denotes the trajectory of point P_1, the red line denotes the trajectory of point P_2. Due to the volume expansion, as shown in Fig. 15(a), we observe that the trajectory by DDA^0 is distorted. By comparing Fig. 15(b) and (c), we can see, the times of contact between the stone and the slope (β = 45°) are once and twice for DDA^1 and $SRDDA_{vp}$, respectively. Moreover, for the sliding distance of the stone, the results by DDA^1 are longer than that by $SRDDA_{vp}$. In addition, from the zoomed views ($zoom_1$, $zoom_2$ and $zoom_3$) in Fig. 15, several turning points of the trajectories can be observed. The corresponding angular velocities can found in Table 7. The potential of $SRDDA_{vp}$ is accordingly demonstrated by the simple example.

5. Conclusions

The S-R decomposition theorem is an important result in the theory

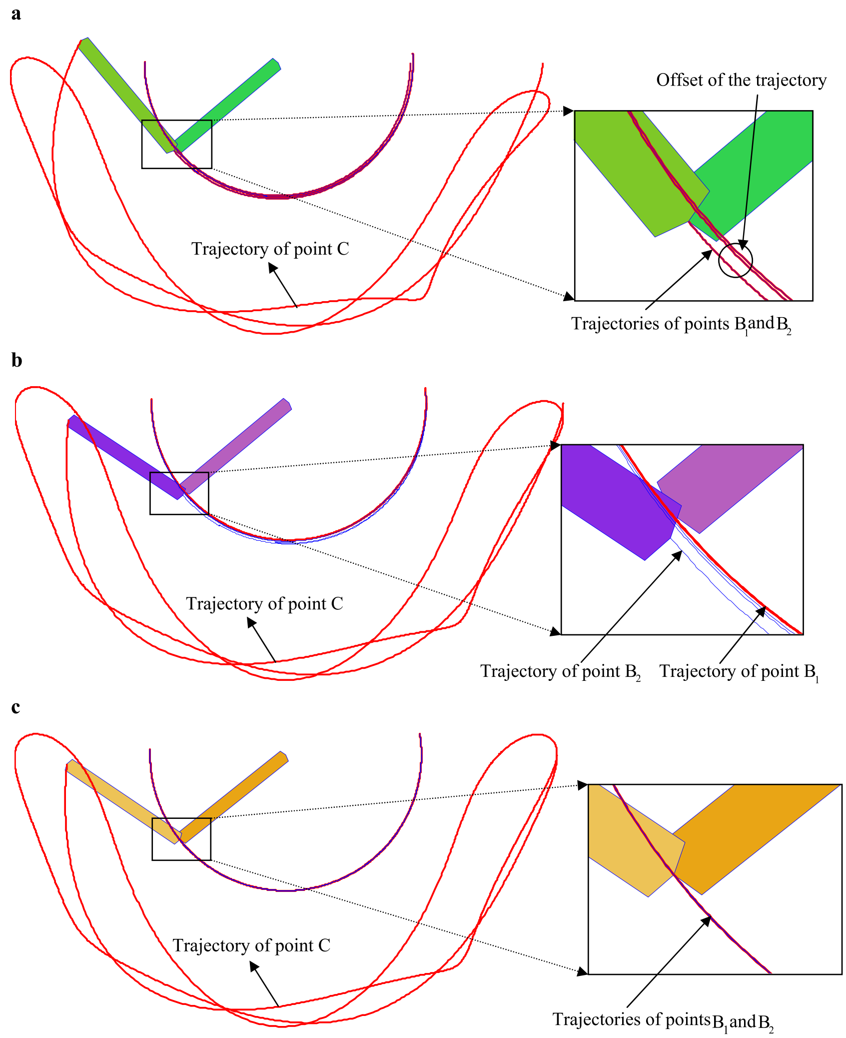

Fig. 12. Angular velocity of a nunchaku given by DDA[1]. (For interpretation of the references to color in this figure legend, the reader is referred to the web version of this article.)

Table 5
Distance between points B_1 and B_2.

CS	DDA^0	DDA^1	$SRDDA_{vp}$
15	0.000000	0.000001	0.000000
100	0.000000	0.000219	0.000000
500	0.000000	0.009848	0.000000
1000	0.000000	0.021701	0.000000
1500	0.000000	0.025308	0.000000
1800	0.000000	0.035775	0.000000

Analytical solution: 0 m. (CS: calculation step)

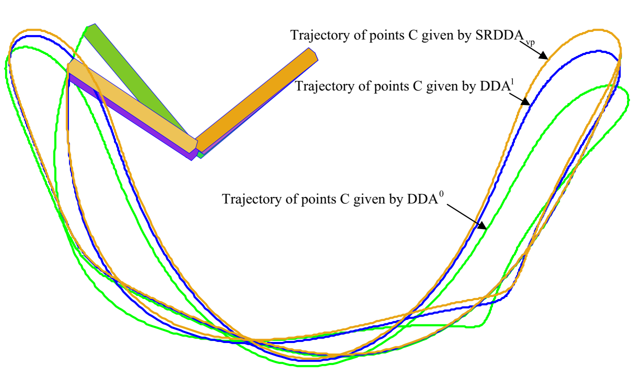

Fig. 13. Trajectories of point C given by DDA^0, DDA^1 and $SRDDA_{vp}$.

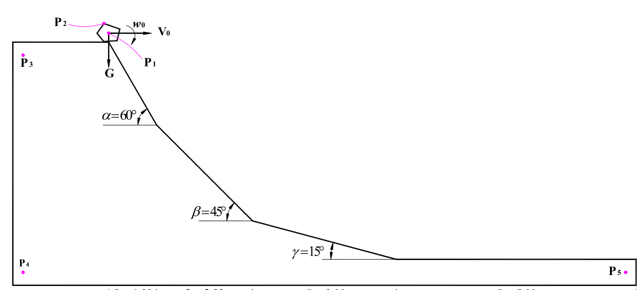

Fig. 14. Configuration of simulation of rockfall.

of geometric nonlinearity. It has an ability to capture strain components and rotation components at the same time. By utilizing this feature, a dynamics formulation was first deduced through the principle of virtual power. Moreover, the update process for the co-moving coordinate, which is closely related to the S-R decomposition theorem, was proposed. The new formulation is independent of the specific numerical methods. Then, in the setting of DDA, an S-R-D-based DDA, abbreviated as $SRDDA_{vp}$, was established. Compared with the conventional DDA, the slightly modified basic unknown variables were adopted in $SRDDA_{vp}$. Some examples have illustrated that $SRDDA_{vp}$ can naturally overcome the issue of volume expansion, effectively improve the calculation accuracy and also equip DDA with the potential to treat large deformation and large rotation.

Table 6
Angular velocity before the first touch (CS =1382) (Fig. 15).

CS	CV (s^{-1})			RE (%)		
	DDA^0	DDA^1	SRDDA$_{vp}$	DDA^0	DDA^1	SRDDA$_{vp}$
100	−1.00000146	−1.00000146	−1.00000033	0.000146	0.000146	0.000033
200	−1.00000271	−1.00000271	−1.00000064	0.000272	0.000272	0.000062
500	−1.00000229	−1.00000229	−1.00000055	0.000229	0.000229	0.000055
800	−1.00000217	−1.00000217	−1.00000043	0.000217	0.000217	0.000043
1000	−1.00000203	−1.00000203	−1.00000040	0.000203	0.000203	0.000040

CS: calculation step; CV: calculation value; RE: relative error.

Table 7
Angular velocity at some CS (Fig. 15).

CS	CV (s^{-1})		
	DDA^0	DDA^1	SRDDA$_{vp}$
1383	-10.25734346 ⊻	-8.85281450 ⊻	-8.85595077 ⊻
1974	-21.31168993 ⊻	-5.61558431 ⩡	-5.78775106 ⩡
2006	-20.83758739 ⩡	-18.34628241 ⊻	-18.55805717 ⊻
2594	-10.85717983 ⩡	-23.45725286 ⊻	-14.94923222 ⩡
2822	-10.85717529 ⩡	-15.69652896 ⩡	14.49043619 ⊻
2913	2.77335470 ⊻	-15.69653176 ⩡	-1.48686482 ⩡

CS: calculation step; CV: calculation value; ⊻: touched; ⩡: not touched.

Acknowledgements

This study is partially supported by the University Grants Council of Hong Kong through a Collaborative Research Fund (CRF) Project C6012-15G. This study is also supported by the National Basic Research Program of China (973 Program), under the Grant no. 2014CB047100; and the National Natural Science Foundation of China, under the Grant nos. 11172313 and 51538001.

Appendix

SRDDA$_{vp}$ for three-dimensional case.

For arbitrary shape three-dimensional block, the shape function becomes

$$\mathbf{T}(x,\ y,\ z)=\begin{bmatrix}1 & 0 & 0 & 0 & z-z_c & y_c-y & x-x_c & 0 & 0 & 0 & (z-z_c)/2 & (y-y_c)/2\\ 0 & 1 & 0 & z_c-z & 0 & x-x_c & 0 & y-y_c & 0 & (z-z_c)/2 & 0 & (x-x_c)/2\\ 0 & 0 & 1 & y-y_c & x_c-x & 0 & 0 & 0 & z-z_c & (y-y_c)/2 & (x-x_c)/2 & 0\end{bmatrix}, \tag{A1}$$

the increment displacement $\Delta\mathbf{u}$ at any point $(x,\ \ y,\ \ z)$ can be given by

$$\Delta\mathbf{u}\ \ (x,\ y,\ z)=\begin{pmatrix}\Delta u\ ^x(x,\ y,\ z)\\ \Delta u\ ^y(x,\ y,\ z)\\ \Delta u\ ^z(x,\ y,\ z)\end{pmatrix}=\mathbf{T}(x,\ y,\ z)\Delta\mathbf{d}_b, \tag{A2}$$

where $\Delta\mathbf{d}\ _b=\{\Delta u,\ \Delta v,\ \Delta w,\ \Delta r_x,\ \Delta r_y,\ \Delta r_z,\ \Delta\varepsilon_x,\ \Delta\varepsilon_y,\ \Delta\varepsilon_z,\ \Delta\gamma_{yz},\ \Delta\gamma_{zx},\ \Delta\gamma_{xy}\}^{\mathrm{T}}$is the generalized increment displacement vector. Δr_x, Δr_y and Δr_z represent the rigid-body rotation angle increments corresponding to x-, y- and z-axis respectively. Moreover, $\Delta\varepsilon_x$, $\Delta\varepsilon_y$, $\Delta\varepsilon_z$, $\Delta\gamma_{yz}$, $\Delta\gamma_{zx}$, $\Delta\gamma_{xy}$ is the six increments strain components. The strain rate increment vector can be chosen as

$$\Delta\dot{\mathbf{S}}(x,\ y,\ z)=\left\{\Delta\dot{S}_1^1,\ \Delta\dot{S}_2^2,\ \Delta\dot{S}_3^3,\ 2\Delta\dot{S}_3^2,\ 2\Delta\dot{S}_1^3,\ 2\Delta\dot{S}_2^1\right\}=\mathbf{B}_b\Delta\mathbf{V}_b, \tag{A3}$$

where

$$\mathbf{B}_b=\begin{bmatrix}0&0&0&0&0&0&1&0&0&0&0&0\\ 0&0&0&0&0&0&0&1&0&0&0&0\\ 0&0&0&0&0&0&0&0&1&0&0&0\\ 0&0&0&0&0&0&0&0&0&1&0&0\\ 0&0&0&0&0&0&0&0&0&0&1&0\\ 0&0&0&0&0&0&0&0&0&0&0&1\end{bmatrix}. \tag{A4}$$

Similarly, the velocity $\mathbf{V}$ reads

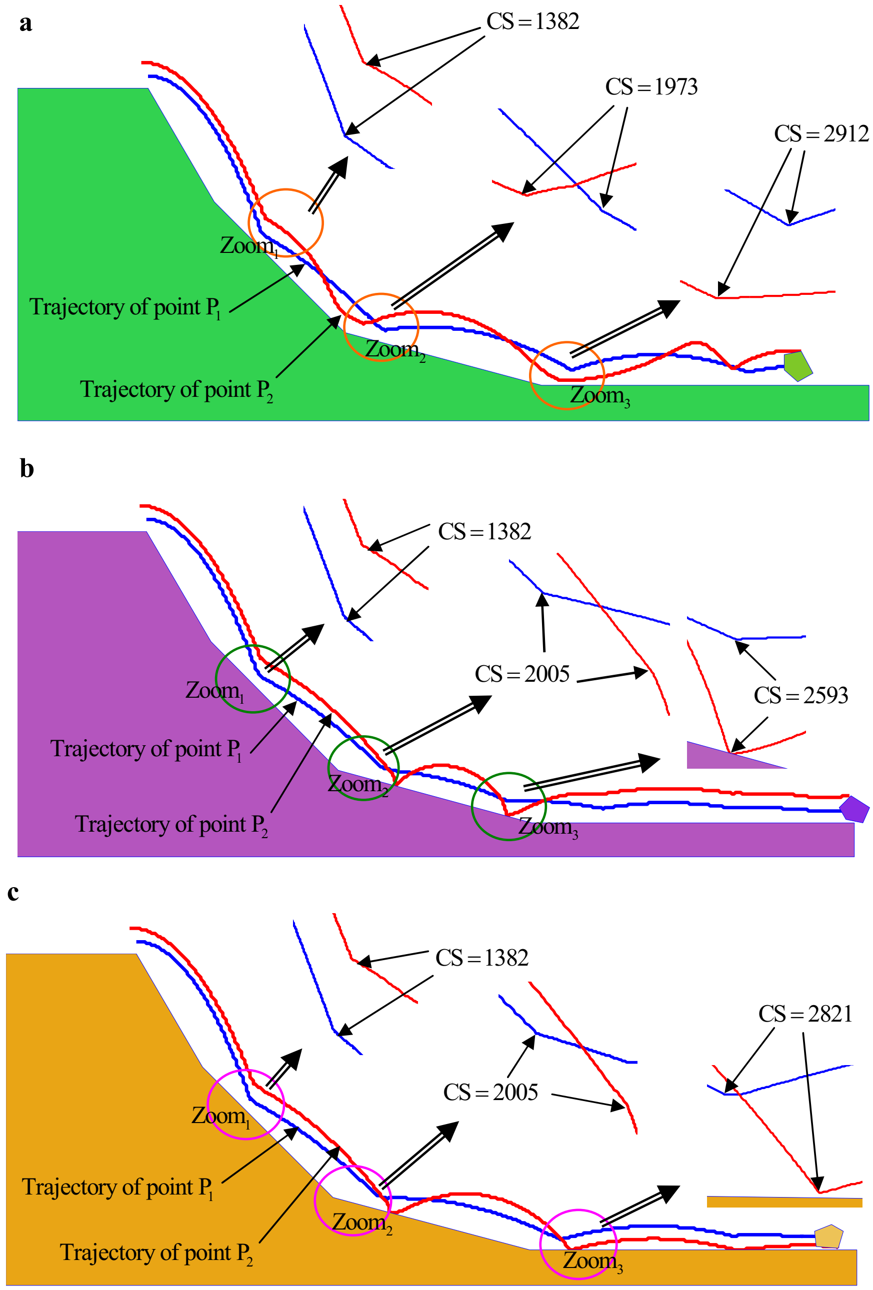

Fig. 15. Trajectories of points P_1 and P_2 given by: (a) DDA^0; (b) DDA^1 and (c) $SRDDA_{vp}$. (For interpretation of the references to color in this figure legend, the reader is referred to the web version of this article.)

$$\mathbf{V}\ (x, y, z) = \begin{pmatrix} v^{\ x}(x, y, z) \\ v^{\ y}(x, y, z) \\ v^{\ z}(x, y, z) \end{pmatrix} = \mathbf{T}(x, y, z)\mathbf{V}_b, \tag{A5}$$

the acceleration $\mathbf{A}$ is

$$\mathbf{A}\ (x, y, z) = \begin{pmatrix} A^{\ x}(x, y, z) \\ A^{\ y}(x, y, z) \\ A^{\ z}(x, y, z) \end{pmatrix} = \mathbf{T}(x, y, z)\mathbf{A}_{\ b}, \tag{A6}$$

where $\mathbf{V}_{\ b} = \{\dot{u}, \dot{v}, \dot{w}, \dot{r}_x, \dot{r}_y, \dot{r}_z, \dot{\varepsilon}_x, \dot{\varepsilon}_y, \dot{\varepsilon}_z, \dot{\gamma}_{yz}, \dot{\gamma}_{zx}, \dot{\gamma}_{xy}\}^{\mathrm{T}}$and $\mathbf{V}_{\ b} = \{\ddot{u}, \ddot{v}, \ddot{w}, \ddot{r}_x, \ddot{r}_y, \ddot{r}_z, \ddot{\varepsilon}_x, \ddot{\varepsilon}_y, \ddot{\varepsilon}_z, \ddot{\gamma}_{yz}, \ddot{\gamma}_{zx}, \ddot{\gamma}_{xy}\}^{\mathrm{T}}$ are the generalized velocity vector and acceleration vector, respectively. And the penalty matrix $\mathbf{k}$ should be

$$\mathbf{k} = \begin{bmatrix} k^{\ x} & 0 & 0 \\ 0 & k^{\ y} & 0 \\ 0 & 0 & k^{\ z} \end{bmatrix}. \tag{A7}$$

Then, the governing equation for three-dimensional case can be easily constructed. And the increment strain is obtained by Eqs. (12), (14) and (15) only need to replace $S_j^{\ i}$, $u^{\ i}|_j$ and θ by $\Delta S_j^{\ i}$, $\Delta u^{\ i}|_j$ and $\Delta\theta$, respectively, reads

$$\Delta S_j{}^i = \frac{1}{2}\left(\Delta u^i|_j + \Delta u\ {}^i|_j^{\mathrm{T}}\right) - \Delta L_k{}^i \Delta L_j{}^k (1 - \cos(\Delta\theta)), \quad i, j, k = 1, 2, 3, \tag{A8}$$

where

$$\Delta L_j{}^i = \frac{1}{2\sin(\Delta\theta)}\left(\Delta u\ {}^i|_j - \Delta u\ {}^i|_j^{\mathrm{T}}\right), \tag{A9}$$

and

$$\sin(\Delta\theta) = \frac{1}{2}\sqrt{\left(\Delta u\ {}^1|_2 - \Delta u\ {}^1|_2^{\mathrm{T}}\right)^2 + \left(\Delta u\ {}^2|_3 - \Delta u\ {}^2|_3^{\mathrm{T}}\right)^2 + \left(\Delta u\ {}^1|_3 - \Delta u\ {}^1|_3^{\mathrm{T}}\right)^2}. \tag{A10}$$

References

1 Shi GH. Discontinuous deformation analysis: a new numerical model for the statics and dynamics of block system [PhD thesis], Berkeley, California: Univ Calif Berkeley; 1988.
2 Shi GH, Goodman RE. Generalization of two-dimensional discontinuous deformation analysis for forward modelling. *Int J Numer Anal Methods Geomech*. 1989;13:359–380.
3 Jing LR. Formulation of discontinuous deformation analysis (DDA)—an implicit discrete element model for block systems. *Eng Geol*. 1998;49:371–381.
4 MacLaughlin MM, Doolin DM. Review of validation of the discontinuous deformation analysis (DDA) method. *Int J Numer Anal Methods Geomech*. 2006;30:271–305.
5 Ning YJ, Zhao ZY. A detailed investigation of block dynamic sliding by the discontinuous deformation analysis. *Int J Numer Anal Methods Geomech*. 2011;37:2373–2393.
6 Wu JH. Seismic landslide simulations in discontinuous deformation analysis. *Comput Geotech*. 2010;37(5):594–601.
7 Wu JH, Chen CH. Application of DDA to simulate characteristics of the tsaoling landslide. *Comput Geotech*. 2011;38(5):741–750.
8 Zhang YH, Fu XD, Sheng Q. Modification of the discontinuous deformation analysis method and its application to seismic response analysis of large underground caverns. *Tunn Undergr Sp Tech*. 2014;40:241–250.
9 Pearce CJ, Thavalingam A, Liao Z, N. Bicanic N. Computational aspects of the discontinuous deformation analysis framework for modelling concrete fracture. *Eng Frac Mech*. 2000;65:283–298.
10 Ning YJ, Yang J, An XM, Ma GW. Modelling rock fracturing and blast-induced rock mass failure via advanced discretisation within the discontinuous deformation analysis framework. *Comput Geotech*. 2011;38(1):40–49.
11 Tian Q, Zhao ZY, Bao HR. Block fracturing analysis using nodal-based discontinuous deformation analysis with the double minimization procedure. *Int J Numer Anal Methods Geomech*. 2013;38(9):881–902.
12 Ben YX, Wang Y, Shi GH. Development of a model for simulating hydraulic fracturing with DDA. In: *Proceedings of the 11th International Conference on Analysis of Discontinuous Deformation*. Fukuoka; 27–29 August 2013. p. 169–175; 2013.
13 Jiao YY, Zhang HQ, Zhang XL, Li HB, Jiang QH. A two-dimensional coupled hydromechanical discontinuum model for simulating rock hydraulic fracturing. *Int J Numer Anal Methods Geomech*. 2015;39(5):457–481.
14 Kamai R, Hatzor YH. Numerical analysis of block stone displacements in ancient masonry structures: a new method to estimate historic ground motions. *Int J Numer Anal Methods Geomech*. 2008;32:1321–1340.
15 Cheng GQ. Numerical simulation in rockfall analysis: a close comparison of 2-D and 3-D DDA. *Rock Mech Rock Eng*. 2013;46:527–541.
16 Jing LR, Ma Y, Fang Z. Modeling of fluid flow and solid deformation for fractured rocks with discontinuous deformation analysis (DDA) method. *Int J Rock Mech Min Sci*. 2011;38:343–355.
17 Ke TC, Bray JD. Modeling of particulate media using discontinuous deformation analysis. *J Eng Mech*. 1995;121(11):1234–1243.
18 Beyabanaki SAR, Bagtzoglou AC. Non-rigid disk-based DDA with a new contact model. *Comput Geotech*. 2013;49:25–35.
19 Chern JC, Koo CY, Chen S. Development of second order displacement function for DDA and manifold method [Vicksburg]. *Work Forum Manifold Method Mater Anal*. 1997:183–202.
20 Shyu K. Nodal-based discontinuous deformation analysis [PhD thesis], California: Univ Calif Berkeley, Berkeley; 1993.
21 Zhang YH, Cheng YM. Coupling of FEM and DDA methods. *Int J Geomech*. 2002;2(4):503–517.
22 Miki S, Sasaki T, Koyama T, Nishiyama S, Ohnishi Y. Development of coupled discontinuous deformation analysis and numerical manifold method (NMM–DDA). *Int J Comput Methods*. 2010;7(1):1–20.
23 Sun Yue, Chen Qian, Feng Xiangchu, Wang Ying. Discontinuous deformation analysis enriched by the bonding block model [2015]. *Math Probl Eng*. 2015:723263.
24 Ke TC. The issue of rigid body rotation in DDA [Berkeley; 12–14 June]Proceedings of the first international forum on discontinuous deformation analysis (DDA) and simulation of discontinuous media, 1996; 1996, pp.318–325.
25 MacLaughlin MM, Sitar N. Rigid body rotation in DDA [Berkeley; 12–14 June] Proceedings of the first international forum on discontinuous deformation analysis (DDA) and simulation of discontinuous media, 1996; 1996, pp.620–635.
26 Cheng YM, Zhang YH. Rigid body rotation and block internal discretization in DDA analysis. *Int J Numer Anal Methods Geomech*. 2000;24(6):567–578.
27 Wu JH, Ohnishin Yuzo, Nishiyama Satoshi. A development of the discontinuous deformation analysis for rock fall analysis. *Int J Numer Anal Methods Geomech*. 2005;29:971–988.
28 Jiang W, Zheng H. An efficient remedy for the false volume expansion of DDA when simulating large rotation. *Comput Geotech*. 2015;70:18–23.
29 Wu JH. The elastic distortion problem with large rotation in discontinuous deformation analysis. *Comput Geotech*. 2015;69:352–364.
30 Jiang QH, Chen YF, Zhou CB. Man-chu Ronald Yeung. Kinetic energy dissipation and convergence driterion of discontinu?Ous deformations analysis (DDA) for geotechnical engineering. *Rock Mech Rock Eng*. 2013;46:1443–1460.
31 Wu JH, Lin HM. Improvement of open-close iteration in DDA [Fukuoka; 27–29 August]Frontiers of Discontinuous Numerical Methods and Practical Simulations in Engineering and Disaster Prevention, 2013; 2013, pp.185–191.
32 Fan H, He SM. An angle-based method dealing with Vertex-vertex contact in the two-dimensional discontinuous deformation analysis (DDA). *Rock Mech Rock Eng*. 2015;48:2031–2043.
33 Lin CT, Amadei B, Jung J, Dwyer J. Extensions of discontinuous deformation analysis for jointed rock masses. *Int J Rock Mech Min Sci*. 1996;33:671–694.
34 Cai YE, Liang GP, Shi GH, Cook NGW. Studying an impact problem by using LDDA method [Berkeley; 12–14 June]. *Proc first Int Forum Disco Deform Anal (DDA) Simul Disco Media*. 1996:288–295.
35 Zheng H, Jiang W. Discontinuous deformation analysis based on complementary theory. *Sci China Tech Sci*. 2009;29:2547–2554.
36 Zheng H, Li XK. Mixed linear complementarity formulation of discontinuous deformation analysis. *Int J Rock Mech Min Sci*. 2015;75:23–32.
37 Li XK, Zheng H. Condensed form of complementarity formulation for discontinuous deformation analysis. *Sci China Tech Sci*. 2015;58(9):1509–1519.
38 Jiang W, Zheng H. Discontinuous deformation analysis based on variational inequality theory. *Int J Comput Methods*. 2011;8:193–208.
39 Bao HR, Zhao ZY. An alternative scheme for the corner-corner contact in the two-dimensional discontinuous deformation analysis. *Adv Eng Softw*. 2010;41:206–212.
40 Shi GH. Theory and examples of three dimensional discontinuous deformation analysis. In: *Proceedings of the 2nd Asian Rock Mechanics Symposium*. Beijing; 11–14 September. p. 27–32; 2001.
41 Jiang QH, Yeung MR. A model of point-to-face contact for three-dimensional discontinuous deformation analysis. *Rock Mech Rock Eng*. 2004;37:95–116.
42 Yeung MR, Jiang QH, Sun N. A model of edge-to-edge contact for three-dimensional discontinuous deformation analysis. *Comput Geotech*. 2007;34:175–186.
43 Wu JH, Juang CH, Lin HM. Vertex-to-face contact searching algorithm for three-dimensional frictionless contact problems. *Int J Numer Methods Eng*. 2005;63:876–897.
44 Beyabanaki SAR, Mikola RG, Hatami K. Three-dimensional deformation analysis (3-D DDA) using a new contact resolution algorithm. *Comput Geotech*. 2008;35:346–356.
45 Liu J, Geng QD, Kong XJ. A fast common plane identification algorithm for 3D contact problems. *Comput Geotech*. 2009;36:41–51.
46 Wu W, Zhu HH, Zhuang XY, et al. A multi-shell cover algorithm for contact detection in the three dimensional discontinuous deformation analysis. *Theor Appl Fract Mech*. 2014;72:136–149.
47 Beyabanaki SAR, Jafari A, Biabanaki SOR, Yeung MR. Nodal-based three-dimensional discontinuous deformation analysis (3-DDDA). *Comput Geotech*. 2009;36:359–372.
48 Shi GH. Contact theory. *Sci China Tech Sci*. 2015;58:1–47.
49 Chen ZD. On the representation of finite rotation in nonlinear field theory of continuum mechanics. *Appl Math Mech*. 1986;7(11):1017–1026.
50 Qin Z, Chen ZD. Large deformation analysis of shells with finite element method based on the S-R decomposition theorem. *Comput Struct*. 1988;30(4):957–961.
51 Chen ZD. Rational Mechanics, China, Xuzhou: China Univ Min Press; 1988 [In Chinese].
52 Li P, Chen ZD. The updated co-moving coordinate formulation of continuum mechanics based on the S-R decomposition theorem. *Comput Methods Appl Mech Eng*. 1994;114:21–34.
53 Chen M, Liang JW, Chen X, Chen ZD. On uniqueness, existence and objectivity of S-